# Structural transformation identification of sputtered amorphous $MoS_x$ as efficient hydrogen evolving catalyst during electrochemical activation

Fanxing Xi, [*,†] Peter Bogdanoff, [*,†] Karsten Harbauer, [†] Paul Plate, [†] Christian Höhn,[†] Jörg Rappich,[‡] Bin Wang,[§] Xiaoyu Han,[⊥] Roel van de Krol,[†] Sebastian Fiechter[*,†]

[†]Helmholtz-Zentrum Berlin für Materialien und Energie GmbH, Institute for Solar Fuels, Hahn-Meitner-Platz 1, 14109 Berlin, and [‡] Institute Silicon Photovoltaics, Magnusstrasse 12, 12489 Berlin, Germany; [§] School of Physics and Electronic Engineerning, Guangzhou University, Waihuanxi Road No.230, Guangzhou 510006, P.R. China, and [⊥]Department of Chemistry, University College London, 20 Gordon Street, London WC1H 0AJ, United Kingdom

*E-mail: fanxing.xi@helmholtz-berlin.de; fiechter@helmholtz-berlin.de*

*Keywords: structural transformation, hydrogen evolving catalyst, molybdenum sulfide, sputtering, water splitting*

**Abstract:** Molybdenum sulfide $MoS_x$ is considered as attractive hydrogen evolution catalyst since it is free of noble metals and shows a low overvoltage. Especially, amorphous molybdenum sulfide has attracted attention because of its high catalytic activity. However, the catalytic mechanism of the hydrogen evolution reaction is not yet fully understood. Therefore in our study, layers of $MoS_x$ were deposited by reactive magnetron sputtering varying the substrate temperature in the range from room temperature (RT) to 500°C. The morphology and structure of the films change significantly as a function of temperature, from an amorphous to a highly textured 2H-$MoS_2$ phase. The highest catalytic activity was found for amorphous layers deposited at RT showing an overvoltage of 180 mV at a current density of -10 $mAcm^{-2}$ in a 0.5 M sulfuric acid electrolyte (pH 0.3) after electrochemical activation. As detected by Raman spectroscopy the RT deposited catalyst consists of $[Mo_3S_{13}]^{2-}$ and $[Mo_3S_{12}]^{2-}$ entities which are interconnected via $[S_2]^{2-}$ and $S^{2-}$ ligands. When sweeping the potential from 0.2 to -0.3 V vs RHE a massive release of sulfur in form of gaseous $H_2S$ was observed in the first minutes as detected by differential electrochemical mass spectroscopy (DEMS). After electrochemical cycling for 10 min, the chains of these clusters transform into a layer-type $MoS_{2-x}$ phase. In this transformation process, $H_2S$ formation gradually vanishes and $H_2$ evolution becomes dominant. The new phase is considered as a sulfur deficient molybdenum sulfide characterized by a high number of molybdenum atoms located at the edges of nano-sized $MoS_x$ islands, which act as catalytically active centers.

## 1 Introduction

Large scale solar energy conversion is a sustainable and environmentally friendly approach to meet the high energy demand of mankind using renewable energies.[1] Since the pioneering work of Boddy in 1968 [2] and later by Honda and Fujishima,[3] who investigated photoelectrochemical water splitting by using $TiO_2$ single crystal electrodes, chemical energy conversion at the semiconductor-electrolyte interface has attracted increasing interest as a promising route to convert solar energy into fuels.[4] Hydrogen as a fuel obtained by solar driven water splitting is of significance, not only because of its high energy density, but also by avoiding further release of $CO_2$ into the atmosphere.

To electrolyze water most efficiently into hydrogen and oxygen at the cathode and anode side, respectively, suitable catalysts are necessary to minimize the overpotentials to drive the reaction.[5] In case of the hydrogen evolution reaction (HER), platinum is known as a highly effective catalyst exhibiting an overpotential of less than 100 mV at a current density of -10 $mAcm^{-2}$.[6] However, as an expensive and rare element its use in mass production and large-scale applications should be avoided if possible.[7] Thus, there is a strong incentive to develop cheap, non-toxic and earth-abundant as well as highly active catalysts as alternatives to platinum in order to produce hydrogen in large quantities. Potential candidate materials include transition metal alloys,[5] phosphides,[8] sulfides,[9] and carbides.[10] Molybdenum disulfide ($MoS_2$) that preferentially crystallizes in a hexagonal layer structure[11] was originally investigated as a catalyst for the hydrodesulfurization of crude oil.[12] It was first identified by Tributsch et al. as a hydrogen evolving catalyst in 1977.[13, 14] Later, other re-

searchers confirmed its promising electrocatalytic and/or photoelectrocatalytic activity for hydrogen evolution and its excellent stability.[15] Highly active $MoS_2$ can be prepared by different synthesis routes. For instance, $MoS_2$ nanoparticles, deposited on a graphite support, were prepared and used as catalyst for electrochemical hydrogen evolution by Hinnemann et al. in 2005.[16] Ager et al. demonstrated in 2016 a thermal treatment that converts inert bulk $MoS_2$ to an active HER catalyst.[17] In 2017, Choi et al. produced $MoS_2$ on carbon fiber paper and investigated the electrocatalytic activity of $MoS_2$ studying the phase transition from amorphous to a crystalline material.[18]

Despite these efforts, the catalytic performance of $MoS_2$ in terms of overpotential, turnover frequency (TOF) and stability is still inferior to platinum. One reason for this is that the adsorption of protons ($H^+$) on molybdenum sulfide is an energetic uphill reaction. Furthermore, the (00.1) surfaces of hexagonal $MoS_2$ particles cannot provide suitable reaction centers to reduce protons; only the edge sites of $MoS_2$ are active in catalyzing the HER.[19] To improve the catalytic ability of molybdenum sulfides, efforts have been made to bring more edge sites in contact with the electrolyte by e.g. structural engineering[20] and by activating non-active basal planes through generation of sulfur vacancies.[21] In addition, amorphous molybdenum sulfide[22] has been studied because the lack of long range order gives the material unique catalytic properties.[23] For instance, Merki et al.[24] prepared amorphous $MoS_x$ thin film catalyst layers electrochemically, which resulted in a significant increase of current density for proton reduction. They reported a current density of -15 $mAcm^{-2}$ at an overpotential of $\eta$ = 200 mV, which is lower than that of the crystalline material. An amorphous $MoS_2$ HER catalyst was also prepared by Shin et al. using atomic layer deposition.[25] However, the catalyzing mechanism of the amorphous material and the reason for its high catalytic activity remain unclear. Therefore, further studies are required to investigate this catalyst in more detail and to identify the catalytically active center(s) in order to further improve its catalytic activity and stability.

In this study, reactive magnetron sputtering in an argon / hydrogen disulfide ($Ar/H_2S$) atmosphere is used to directly deposit molybdenum sulfides on fluorine-doped tin oxide (FTO) substrates in a fast and homogeneous way. This technique allows molybdenum sulfides with different degrees of crystallinity to be produced by simply varying the substrate temperature. The relationship between the catalytic properties of molybdenum sulfide films and its crystallinity was studied by electrochemical measurements combined with Raman and X-ray photoelectron spectroscopy (XPS). The highest catalytic activities have been achieved after electrochemical activation of amorphous $MoS_x$ films, which were sputtered at room temperature (RT). Different sulfur species, such as bridging and terminal $[S_2]^{2-}$ units typically known from crystalline cluster compounds like $(NH_4)_2Mo_3S_{13}$, were found to exist in the as-prepared material. [26] We find that the RT sputtered amorphous $MoS_x$ films experience a structural transformation during electrochemical cycling, changing from an amorphous material consisting of $Mo_3S_{13}$ or $Mo_3S_{12}$ entities to $MoS_2$-like nano-islands. After this structural transformation, the $MoS_x$ electrode acquires a good catalytic performance as HER catalyst with strongly reduced overpotential of 180 mV at a current density of -10 $mAcm^{-2}$ ($\eta_{10}$) and good stability over 10 h during electrochemical cycling in a 0.5 M sulfuric acid electrolyte.

## 2 Experimental

### 2.1 Preparation of molybdenum sulfide electrodes

Molybdenum sulfide electrodes were prepared by reactive magnetron sputtering (see scheme shown in SI Figure S1). A molybdenum target (99.99%, Freiberger NE-Metall GmbH) was used during the sputtering process with an output power of 100 W DC in $H_2S$/Ar atmosphere ($H_2S$ : Ar ratio = 3:1, flow rate $H_2S$ : Ar = 5.1 sccm : 1.7 sccm, total pressure P ≈ 1.3 Pa) to produce the sputtering plasma. The substrate temperatures varied from room temperature to 500 °C. Before each deposition the metal target was pre-sputtered for 5 min. The FTO substrates were 2.2 cm * 2.2 cm in size. All the substrates were cleaned in acetone, ethanol, and deionized water for 20 min in an ultrasonic bath and dried in $N_2$ gas flow before sputtering.

$(NH_4)_2Mo_3S_{13}$ was synthesized according to a synthesis described by Müller et al.[27] In a round flask (250 mL) $(NH_4)_6Mo_7O_{24}\bullet 4H_2O$ (4 g) was dissolved in deionized water (20 mL). A solution of ammonium polysulfide (120 mL, 8%, Fisher Scientific) was added and heated under reflux overnight (90 °C). A dark-red precipitate ($(NH_4)_2Mo_3S_{13}$) was formed which was filtered and washed with ethanol and water afterwards. Subsequently, the powder was annealed at 80 °C in toluene (50 mL) for about 2 h. After filtering and drying, the dark red thiomolybdate powder was obtained. To prepare thin films of the material, the prepared powder was dissolved in dimethyl sulfoxide (DMSO) and deposited by spin-coating on FTO glass substrates.

### 2.2 Structural Characterization

The morphology of the films was measured by field emission scanning electron microscopy (FESEM) using a LEO GEMINI 1530 instrument from ZEISS, operated with an acceleration voltage of 5 kV. X-ray photoelectron spectroscopy (XPS analyzer from SPECS, PHOIBOS 100) with a monochromatic X-ray source (SPECS FOCUS 500 monochromator, Al Kα radiation, 1486.74eV) was used to study the composition and the valence state of the elements. The data were calibrated using the carbon peak at 284.5 eV. Raman spectra of the samples were measured by two systems: an XploRA system from Horiba (λ = 532 nm, light intensity 0.112 mW) and a DILOR LabRAM micro Raman system for *in-situ* measurements (λ = 632.8 nm, light intensity 4.3 $mW/mm^2$ (D2) or 47.1 $mW/mm^2$ (D1)). The set-up of the *in-situ* Raman cell is shown in the Supplementary Information, Figure S2. A Bruker AXS D8 Advance X-ray diffractometer with Cu Kα radiation (λ = 0.15406 nm) was used to obtain glancing incidence X-ray diffractograms (GIXRD). The angle of incidence was 0.5°

and the measured detection angle (2θ) was varied from 5° to 70°.

2.3 Electrochemical measurements

The electrochemical measurements were performed with a VersaSTAT potentiostat in a three-electrode configuration. $MoS_x$ films deposited on FTO were used as working electrodes (WE) while an Ag/AgCl electrode in saturated KCl solution (-0.197 V vs. reversible hydrogen electrode (RHE)) was used as reference electrode (RE), and a platinum wire served as counter electrode (CE). The electrolyte used was aqueous solution of 0.5 M $H_2SO_4$ (pH 0.3). The contacting area of the sample with the electrolyte was fixed using an O-ring with a diameter of 0.55cm. The iR drop in the electrolyte was calculated by measuring the resistance of the sample in the electrolyte at 100 kHz using electrochemical impedance spectroscopy (EIS) with a modulation frequency of 10 mV. The current density was evaluated from cyclic voltammetry (CV) measurements. The CV measurements were performed within the potential range from 0.2 V to -0.3 V vs RHE with a scan rate of 10 mV/s. The capacitance measurements were performed by sweeping the potential from 0.1 V to 0.31 V vs RHE using different scan rates (10 mV/s to 160 mV/s).

Differential electrochemical mass spectroscopy (DEMS) was employed to measure gases released during the electrochemical measurements. The DEMS system consists of a three-electrode electrochemical cell and a differentially pumped vacuum system attached to a mass spectrometer (QMG 220 M1, PrismaPlus 1-100 amu). A porous hydrophobic membrane was put in between the pumping system and the working electrode in the cell. The scheme of the DEMS cell is shown in the Supplementary Information, Figure S3. Using this geometry, the gases produced at the working electrode need to diffuse through only 200 μm of electrolyte in front of the working electrode and the membrane and then be sucked into the vacuum system to be measured by the mass spectrometer. Further details can be found in a previous paper.[28]

3 Results and discussions

3.1 Preparation of $MoS_x$ films

The morphology of the molybdenum sulfide films deposited on FTO substrates for 5 min. using reactive magnetron sputtering at different substrate temperatures was investigated by SEM (see Fig. 1). When sputtered at room temperature, uniform films of molybdenum sulfide with 350 nm thickness were formed (see Figs. 1A and 1B). Films sputtered at room temperature are dense and homogeneous with a specular and grey optical appearance. As the sputtering temperature increases to 100 °C, leaf-like flakes begin to grow on a dense amorphous bottom layer as shown in Figs. 1C and 1D. The film becomes darker and opaque when sputtered at temperatures higher than 150 °C. In addition, a double-layer structure of molybdenum sulfide film forms, the morphology of which is shown in Figs. 1E and 1F. The top layer of the molybdenum sulfide is black and porous characterized by upright standing dendritic leaf-like crystallites. When carefully removing the top layer of these films, a silver shining molybdenum sulfide bottom layer appears with metallic luster as known from the mineral molybdenite (see also Fig. S4). The "thickness" of the porous film is about 450 nm according to the cross section SEM.

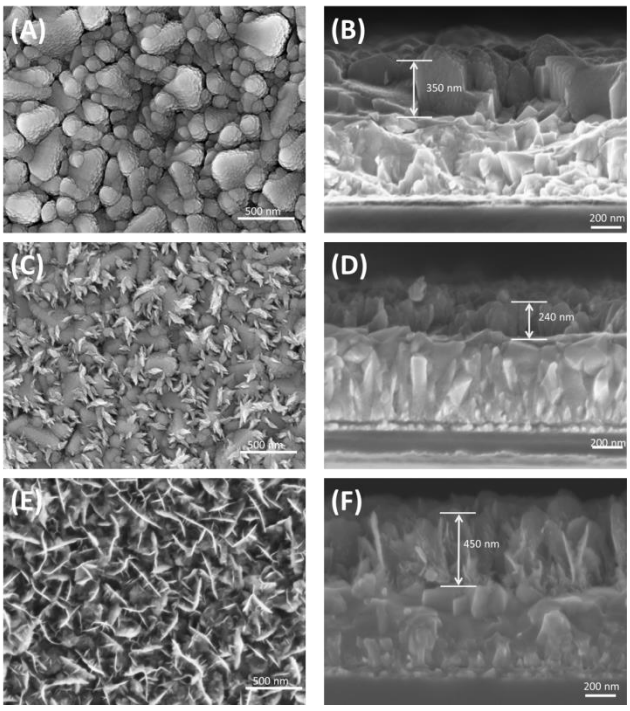


Figure 1. Left column shows top views, the right column side views of molybdenum sulfide films deposited on FTO glass by reactive magnetron sputtering for 5 min at room temperature (A and B), at 100 °C (C and D), and at 500 °C (E and F).

X-ray diffractograms of $MoS_x$ films sputtered at different substrate temperatures are shown in Fig. 2A. When sputtered at room temperature, only one broad molybdenum sulfide peak at 13.8° can be observed suggesting a mostly amorphous film. As the sputtering temperature increases to a temperature higher than 150 °C, the peak at 13.8° increases in intensity, indicating improved crystallinity in the material. Additional diffraction features appear at 2θ = 33°, 58°, which indicate a (01.0) orientation and (11.0) lattice planes parallel to the substrate. Their appearance is associated with the presence of upright standing $MoS_x$ nanoflakes, which can be explained by (hk.0) texture of 2H-$MoS_2$ nanocrystals. Below the porous black film a silver shining $MoS_2$ bottom layer is located which becomes visible after removal of the top porous layer (SI Fig. S4). The bottom layer has a (00.1) texture as shown in SI Fig. S5 since the sample deposited at 500°C without top porous layer only shows one peak at 13.8 ° with higher intensity other than peaks from FTO. The thickness of the bottom layers were determined from the FWHM values of the 00.2 peak at 2θ = 13.8° (see Fig. 2A and Fig. S6A). Accordingly, the length of the particles of the porous layer was determined from the 01.0 reflections (SI Fig. S6B)

To elucidate different Mo-S and S-S vibrations in the films, Raman spectra were measured to characterize different molybdenum sulfide samples (Fig. 2B). Films sputtered at 500°C show vibrational modes ($E^1_{2g}$ mode at 376 $cm^{-1}$ (in-plane Mo-S mode) and an $A_{1g}$ mode at 401 $cm^{-1}$

(out of plane S-S mode) which are characteristic for layer compounds.[29] However, the characteristic vibration signals for 2H-$MoS_2$ are relatively small in the room temperature sputtered molybdenum sulfide film. As we can see from the pink curve of RT sputtered $MoS_x$, vibrations of terminal $[S_2]^{2-}$ ($\nu(S\text{-}S)_{te}$) at about 510 $cm^{-1}$) and bridging $[S_2]^{2-}$ ($\nu(S\text{-}S)_{br}$) at 542 $cm^{-1}$) are present which are typical for $[Mo_3S_{13}]^{2-}$ cluster units.[30]

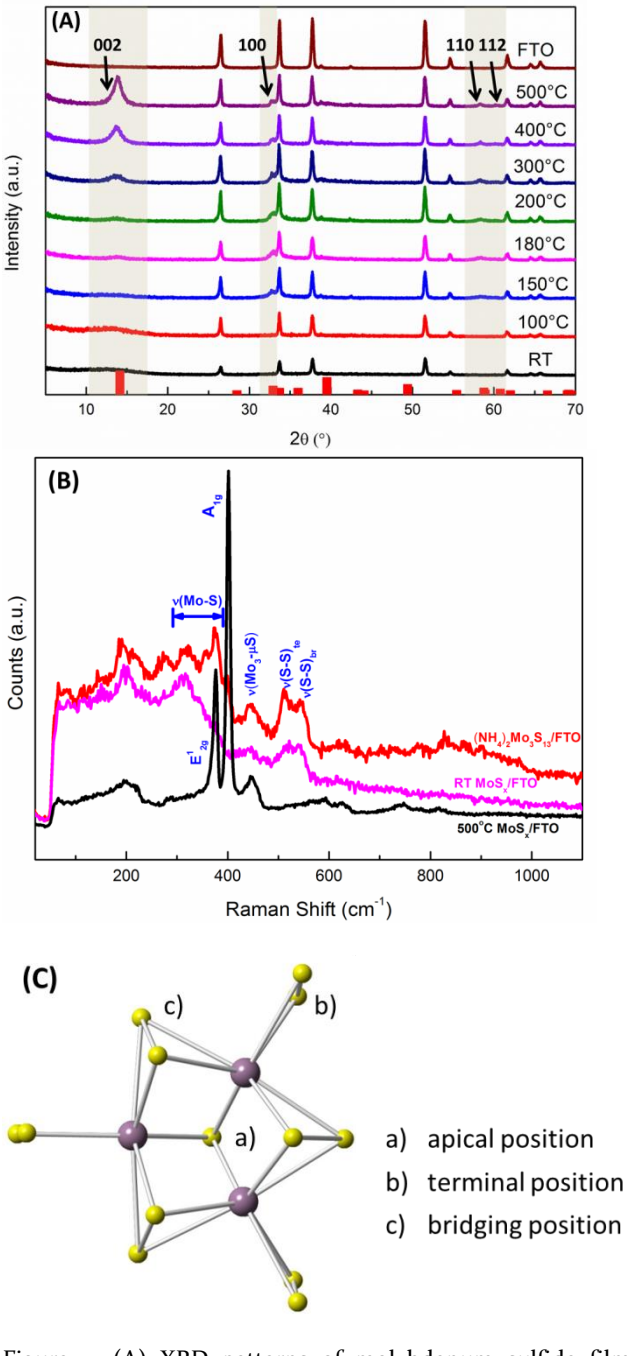


Figure 2. (A) XRD patterns of molybdenum sulfide films deposited by reactive magnetron sputtering at different substrate temperatures as well as the $MoS_2$ standard pattern shown by red bars on the bottom, (B) Raman spectra of different molybdenum sulfide films, (C) characteristic structure of a $[Mo_3S_{13}]^{2-}$ cluster unit (purple balls – molybdenum, yellow balls – sulfur atoms) showing different sulfur bonds.

The high activity of $[Mo_3S_{13}]^{2-}$ as a hydrogen evolving catalyst was first described by Kibsgaard et al. in their 2014 study on $(NH_4)_2Mo_3S_{13}$.[26] It is suggested that the presence of terminal and bridging $[S_2]^{2-}$ in $(NH_4)_2Mo_3S_{13}$ leads to its high HER catalytic activity.[26] The two peaks of terminal disulfide units ($\nu(S\text{-}S)_{te}$) and bridging counterparts ($\nu(S\text{-}S)_{br}$) in our RT sputtered $MoS_x$ are less pronounced than in the $(NH_4)_2Mo_3S_{13}$ spectrum (red curve in Fig. 2B) because of a high degree of amorphicity of $MoS_x$ films sputtered at room temperature: the surrounding environment and the bondings between molybdenum and sulfur are less defined than in $(NH_4)_2Mo_3S_{13}$. The structure of the $[Mo_3S_{13}]^{2-}$ cluster in $(NH_4)_2Mo_3S_{13}$ is depicted in Fig. 2C. From the resemblance of the Raman spectra it can be concluded that films deposited by reactive magnetron sputtering at RT have structural similarities with films prepared from a $(NH_4)_2Mo_3S_{13}$ solution.

### 3.2 Electrocatalytic performance

The catalytic activity of each $MoS_x$ electrode deposited at different substrate temperatures is electrochemically investigated using cyclic voltammetry. Polarization and Tafel curves as shown in Fig. 3 were measured in the voltage range starting from 0.2 V to -0.3 V vs. RHE. Figure 3A shows the result of the voltammetric measurements. Interestingly, an improvement of the current density was noticed during first 10 min of cycling with electrodes deposited at RT and 100 °C. No further improvement was observed after longer electrochemical treatment. This behavior is interpreted as an activation step of the HER electrodes. In addition, the electrochemical behavior of un-activated $MoS_x$ electrodes is displayed in Fig. 3A as dashed lines characterized by higher overpotentials compared to the activated electrodes (black and red curves in Fig. 3A). Tafel slopes were determined from E (V) vs. log(-j) Tafel curves (Fig. 3B). The overpotentials (η) of the electrodes at current densities of -5 $mAcm^{-2}$ and -10 $mAcm^{-2}$ were taken from these curves and are summarized in Figure 4 along with calculated values of the Tafel slopes after curve fitting.

The polarization curves reveal that the overpotentials increase with increasing deposition temperatures. In the crystalline $MoS_2$, the catalytic activity is attributed to atoms located at the edge of the S-Mo-S layer units. The activity (i.e., current density at fixed potential) is therefore expected to increase proportional with the number of active sites at these edges assuming that they are all accessible by the electrolyte. This effect can be explained assuming a decreasing number of sulfur defects (i.e. coordinatively unsaturated bonds of Mo atoms at the edges of S-Mo-S slabs) with increasing substrate temperature during sputtering. These defects are thought to be located at the (hk.0) facets of the crystallites acting as catalytically active centers (see discussion below), which appear as white lines of the upright standing crystallites in Fig. 1E. A rough estimation of the edge length was done for samples prepared at 150 °C and 500 °C for comparison (see SI Figure S7). The total edge lengths of the samples sputtered at 150 °C and 500 °C are 22.1 µm and 14.8 µm, respectively, in an area of 1.41 $µm^2$. This means that a sample prepared at 500°c has much fewer active sites than the sample prepared at 150 °C. Meantime, from Figures S6 A and B the particles in films grown at temperatures above 300°C

exhibit enlarged basal planes as evident from the increasing length *l* which varies from 10 nm to 23 nm for upright standing crystallites in the films grown at temperature in the range 300°C to 500°C. However, the platelet thickness only varies from 6 nm to 6.7 nm in this temperature range. This leads to an overall lowering of the total (01.0) facet area where the catalytic centers are located.

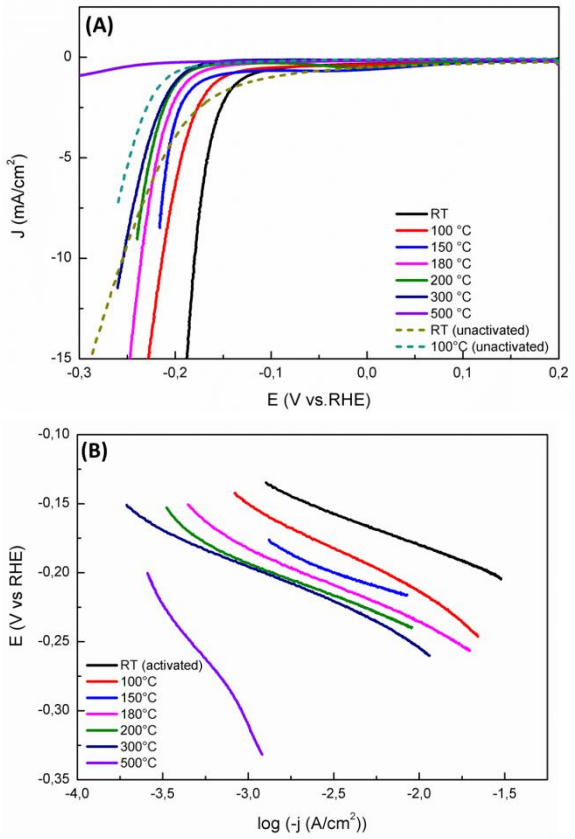


Figure 3. (A) Polarization curves of molybdenum sulfide electrodes sputtered at different temperatures; (B) Tafel plots of the same electrodes.

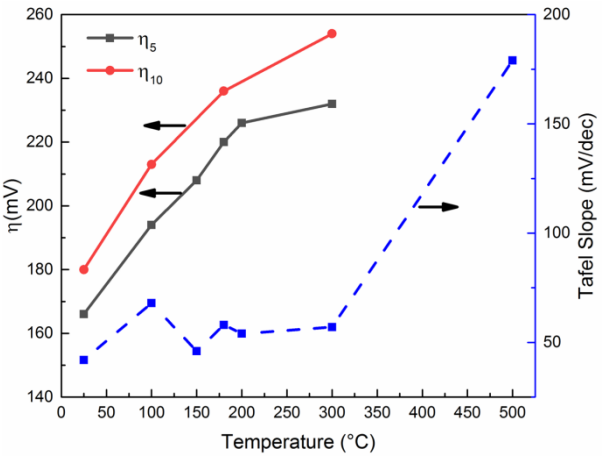


Figure 4. Overpotentials and Tafel slopes of $MoS_x$ sputtered at different substrate temperatures.

Another reason for the increase in overpotential with increasing growth temperature could be the decreasing number of crystal imperfections and sulfur defects that could give rise to coordinatively unsaturated atoms (i.e. active centers).The best catalytic performance has been achieved for $MoS_x$ electrodes deposited at room temperature. The overpotential of 180 mV at a current density of -10 mA/cm² for these electrodes is amongst the lowest ever reported for this material[17, 21, 31].

To explain the changes of the Tafel slopes, the reaction mechanism of the hydrogen evolution reaction has to be taken into account [32]. The elementary surface reactions are:

proton reduction according to the *Volmer step*:

$$H^+ + e^- + * \rightarrow H^* \qquad \text{eq. (1)}$$

with a Tafel slope $b = 2.3RT/\alpha F \approx 120$ mV,

hydrogen desorption according to the *Heyrovsky step*:

$$H^+ + e^- + H^* \rightarrow H_2 + * \qquad \text{eq.(2)}$$

with $b = 2.3RT/(1+\alpha)F \approx 40$ mV,

or according to the *Tafel step*:

$$2H^* \rightarrow H_2 + 2^* \qquad \text{eq. (3)}$$

with $b = 2.3RT/2F \approx 30$ mV.

In these equations (1) (2) and (3), the asterisk * represents a reactive surface site ready to react with hydrogen, R is the ideal gas constant (8.314 $JK^{-1}mol^{-1}$), T the absolute temperature (in Kelvin) and α is related to the barrier symmetry factor, which is about 0.5 for metals.[33]

Although the correlation between the Tafel slope and the HER mechanism was developed for metal surfaces, Tafel analysis can still be used to determine the rate-limiting step during the hydrogen producing process.[34] For instance, Pt has a Tafel slope of 30 mV/decade which means that hydrogen evolution can be explained by the Volmer-Tafel mechanism in which the Tafel reaction is the rate-limiting step [35]. In our study, $MoS_x$ samples prepared at temperatures ranging from room temperature to 300 °C have similar Tafel slopes ranging from 40 to 60 mV/decade. It shows that electrodes prepared in this temperature range show similar reaction mechanisms and the rate limiting step cannot be the Volmer step. However, when the sputtering temperature increases to 500 °C, the Tafel slope increases to 179 mV/decade, which indicates, that the rate limiting step is now likely to be the Volmer step. As discussed above, a possible reason for this change could be that sulfur-dominated basal planes (van der Waals planes) of the hexagonal crystallites contain less edge sites. More experiments are needed to find out the reason for the change of rate-limiting step.

Since platinum was used as counter electrode, we considered the possibility that some Pt could have been dissolved in the electrolyte and was re-deposited on the surface of the $MoS_x$ electrode. To check this, a Pt 4f XPS spectrum was measured for $MoS_x$ sample after 2h of elec-

trochemical cycling in the same potential range from 0.2 V to -0.3 V. No traces of platinum could be found (see SI Fig. S8). In addition, a current-voltage curve of a bare FTO substrate was measured after cycling the electrode for half an hour under the same conditions. Also here, no additional signs for hydrogen evolution could be found (see SI Fig. S9). If Pt had been dissolved in electrolyte and deposited on the cathode surface, a significant increase in hydrogen evolution should have been observed. Therefore, these two measurements prove that FTO itself is not catalytically active and that no Pt has been deposited on the $MoS_x$ electrodes during cycling.

The concentration and the intrinsic activity of the active surface sites are two crucial parameters that determine the overall performance of an electrode. In our study, capacitance measurements through cyclic voltammetry were used to measure the electrochemically active surface area (ECSA) and to further estimate and compare the number of active surface sites. First, the non-faradaic capacitive current of each sample prepared at a specified temperature was measured in the potential range from 0.1 V to 0.31 V vs. RHE. In this potential region, no electrochemical reactions are observed. Under these conditions, the capacitive current is given by the total double layer capacitance, $C_{dl}$ (in F), and the scan rate (ν):[36]

$$i \propto C_{dl} \cdot \nu \qquad \text{eq. (4).}$$

Since the ECSA is proportional to the double layer capacitance, its value can be estimated from $C_{dl}$ measurements obtained by cyclic voltammetry.[37] These measurements were done at different scan rates ranging from 10 mV/s to 160 mV/s for electrodes prepared at different temperatures. The cyclic voltammogram of a room temperature sputtered $MoS_x$ electrode is shown in Figure 5A. An example of the difference between anodic and cathodic current density (Δj) at 0.225 V vs. RHE as a function of scan rate is displayed in Figure 5B for a sample deposited at RT. The slope of Δj vs. scan rate is equal to $2C_{dl}$.[37]

Figure 5C shows the $2C_{dl}$ capacitance as a function of sputtering temperature. The ECSA is proportional to this value and is found to decrease with increasing sputtering temperature. The activated RT sputtered $MoS_x$ has a much higher ECSA, but the ECSA value decreases dramatically as the deposition temperature increases and becomes relatively constant when the temperature reaches 180 °C.

The intrinsic catalytic activity (ICA) of an electrode is proportional to the current density divided by the specific surface area. Here, we define the ICA as the current density at -0.2 V vs. RHE divided by $2C_{dl}$ (since $C_{dl}$ is proportional to the ECSA). Fig. 5D shows the ICA of our $MoS_x$ electrodes as a function of deposition temperature. Its value increases sharply with deposition temperature until a temperature of 300°C, after which the ICA dramatically decreases to the smallest of all values at 500°C. We interpret these results by an increasing activity of the catalytic centers while their concentration decreases with increasing deposition temperature. At temperatures above 300 °C the facets, where these active centers are located, obviously disappear leading to a sharp drop of the catalytic activity.

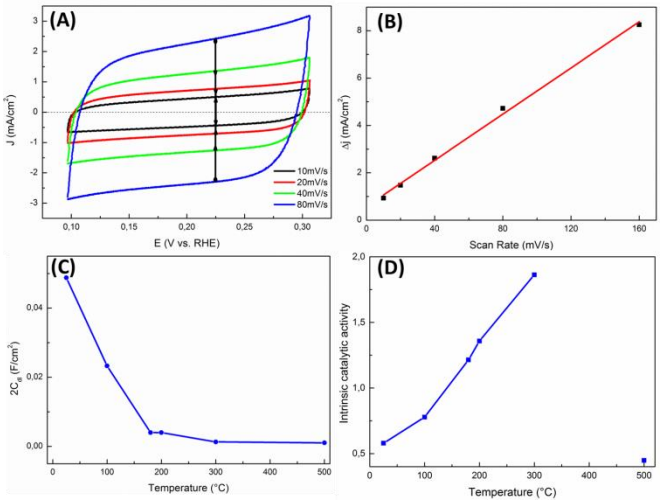


Figure 5. (A) Cyclic voltammograms of amorphous $MoS_x$ measured at different scan rates after activation; (B) Δj plotted as a function of scan rate; (C) $2C_{dl}$ plotted as function of sputtering temperature; (D) current density of the electrodes at -200 mV vs. RHE divided by $2C_{dl}$ and plotted as a function of sputtering temperature.

In addition to a high activity, long term stability is an essential requirement for all catalysts. We tested the stability of $MoS_x$ electrodes sputtered at RT performing CV measurements in the potential range from 0.2 V to -0.3 V vs. RHE at a scan rate of 10 mV/s for ten hours while monitoring the overvoltage needed to produce a current density of -10 $mAcm^{-2}$. Fig. 6 shows the result of the stability test, which is not iR corrected. In the first few minutes, the overpotential decreases from -0.219 V to -0.209 V (see Fig. 6). This improvement corresponds to an activation of the electrode as mentioned above. Afterwards, the overpotential increases steadily, but slowly with time. At the end of the test, the overpotential amounts to -0.255 V, which corresponds to an increase in overpotential of 4.6 mV/h.

One reason for the loss in catalytic activity with time could be a delamination of parts of the electrode layer caused by $H_2$ bubble formation which evokes a decrease of the catalytic activity. SI Figure S10 indeed shows thinning of the $MoS_x$ layer after electrochemical cycling. Furthermore, exposure of the FTO substrate to the electrolyte due to crack formation also can cause loss of catalytic performance (SI Fig. S11).

The catalytic properties of the RT sputtered $MoS_x$ films are far superior to those of films prepared at higher substrate temperatures. The remainder of this paper will, therefore, focus on the amorphous electrode, especially on its activation step. Its properties are further studied in detail by DEMS, *in-situ* and in-line Raman as well as by XPS.

3.3 Electrochemical activation of RT sputtered $MoS_x$

DEMS measurements

Figure 7A shows the first three CV scans of a typical RT sputtered $MoS_x$ electrode without iR correction. The current density of the electrode at – 0.3 V increases from 13 $mAcm^{-2}$ to 22 $mAcm^{-2}$, which means that the catalytic activity of the electrode significantly improves during the first three cycles. No significant increase of the current is observed in subsequent cycles.

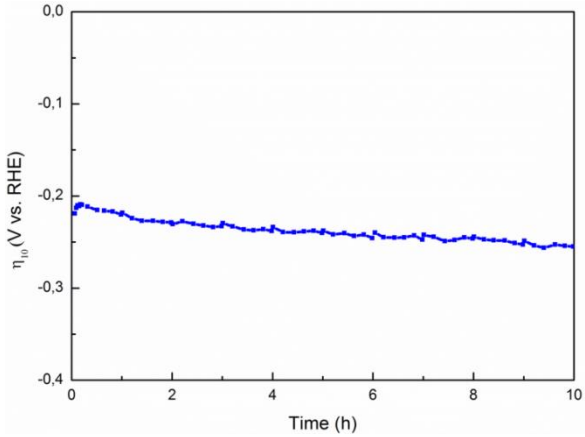


Figure 6. Overpotential of an amorphous $MoS_x$ electrode, deposited at RT, at a current density of -10 $mAcm^{-2}$ continuously sweeping the potential between 0.2 V and -0.3 V vs. RHE for a period of 10 hours.

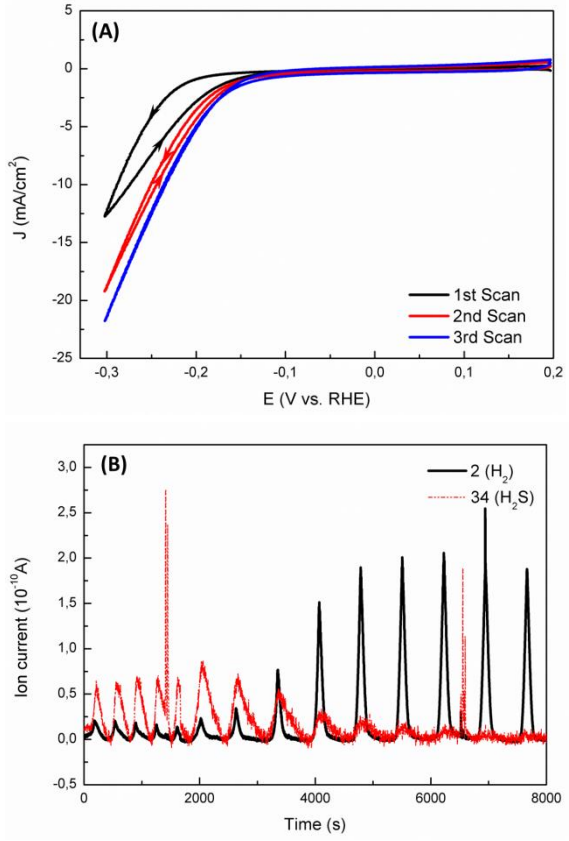


Figure 7. (A) First three CV scans of an amorphous $MoS_x$ electrode deposited at RT; (B) DEMS result of amorphous layer.

To further study this electrode activation, gas evolution at the electrode was investigated by DEMS. The result is shown in Figure 7B. The signals of $H_2^+$ (mass/charge (m/q) = 2) and $H_2S^+$ (m/q = 34) were monitored as a function of time while cycling the electrode between 0.2 V and -0.2 V vs. RHE. During the first 30 minutes, the scan rate was kept constant at 2 mV/s, afterwards it was changed to 1 mV/s. The two spikes in the red curve after 1400 s and 6500 s appear after refreshing the electrolyte. We tentatively attribute their presence to a small fraction of oxygen $^{18}O$ (natural abundance: 0.2%) in the form of $^{16}O$-$^{18}O$ molecules (m = 34 g/mol) that are dissolved in the refreshed electrolyte. The electrolyte is degassed within a minute or so, after which the spikes disappear. In the first hour of measurement, the $H_2S^+$ signal is relatively high, after which it gradually decreases. During the decline of the $H_2S^+$ signal, the peak value of $H_2^+$ starts to increase and saturates after ~4800 s at a level that is ten times higher than in the beginning of the measurement. The $H_2S^+$ peak almost completely disappears. These results indicate that ′activation′ of the electrode is accompanied by loss of sulfur in form of $H_2S$. The activation process takes longer than in the CV scans of Fig. 3 due to the ~10 times lower current densities during the DEMS measurements, which is due to the high ohmic losses in the DEMS cell.

X-ray photoelectron spectroscopy XPS

To investigate the amorphous $MoS_x$ electrode deposited at RT and to study in detail its chemical changes during electrochemical cycling X-ray photoelectron spectroscopy XPS was employed. The cycling consisted of repeated sweeps between 0.2 V and -0.3 V vs. RHE at 10 mV/s.

Figs. 8 A and B show the XPS spectra of Mo 3d and S 2s of the as-prepared $MoS_x$ film before electrochemical treatment. The Mo : S ratio calculated from the spectra equals 1 : 3.97, which is in concordance with the structure of $Mo_3S_{13}$ and/or $Mo_3S_{12}$. The difference between these clusters is a missing apical sulfur atom in the latter cluster (see Fig. 2C and ref. [1]). The peak positions of the Mo $3d_{5/2}$ and $3d_{3/2}$ at 229.1 eV and 232.2 eV, respectively, are indicative of $Mo^{4+}$. The S 2p spectrum of the as-prepared $MoS_x$ reveals the presence of different sulfur ligands bonded to molybdenum, as is known from the $Mo_3S_{13}$ cluster. According to Weber et al., [38, 39] the sulfur ligands with a S $2p_{3/2}$ peak at 161.8 eV can be assigned to terminal $S_2^{2-}$ units and the sulfur peak at 162.9 eV to bridging sulfur. This result agrees well with the above discussed Raman spectra (Fig. 2B, pink curve) of amorphous $MoS_x$. In our measurements, a small but clear third sulfur peak was found at 163.1 eV. This species indicates the presence of a further sulfur species in amorphous $MoS_x$ layers.

Fig. 8 C and D show the XPS spectra after 10 min of electrochemical cycling. The Mo : S ratio now amounts to 1 : 1.89, indicating that a significant fraction of the sulfur atoms near the surface were lost during the electrochemical cycling. This is consistent with the release of sulfur in the form of $H_2S$ that we observed with DEMS (see Fig. 7B).

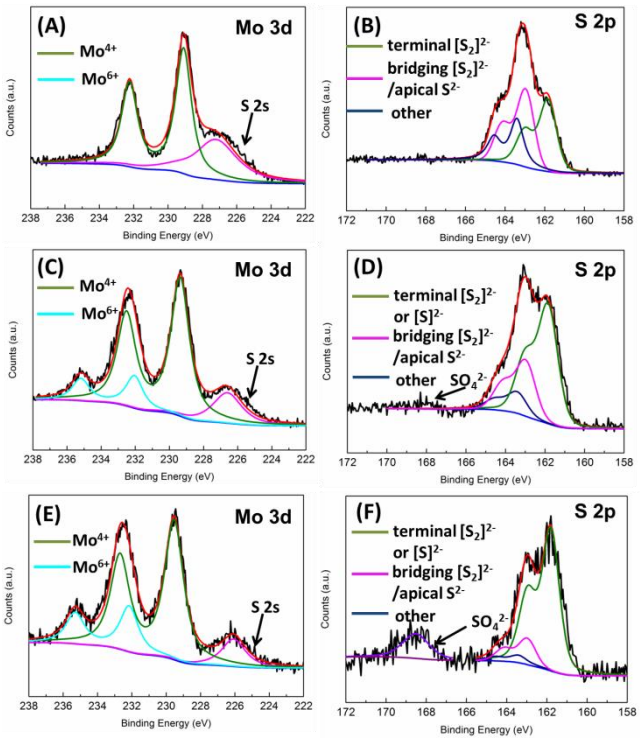


Figure 8. XPS spectra of Mo 3d and S 2s: spectra (A) and (B) belonging to an as-prepared $MoS_x$ film; spectra (C) and (D) to a $MoS_x$ film after electrochemical cycling for 10 min; spectra (E) and (F) related to a $MoS_x$ film after electrochemical cycling for 2 h.

From the fit of S 2p signal in Figure 8D we see a significant decrease of bridging $S_2^{2-}$ species and of the third sulfur species in the cluster units. In addition, the peak position of $Mo^{4+}$ $3d_{5/2}$ shifts from 229.1 eV to 229.3 eV. On the other hand, the cyan curve with $3d_{5/2}$ peak at about 232.5 eV in Fig. 8C indicates the presence of $Mo^{6+}$ in the layer after electrochemical treatment. The appearance of $Mo^{6+}$ can be explained by the oxidation of the electrode surface to $MoO_3$ while being exposed to air during the transport from electrochemical cell to the XPS chamber.

After two hours electrochemical cycling the Mo : S ratio further increases to 1 : 1.35 (Figs. 8 E and F). The Mo $3d_{5/2}$ peak shifts to 229.5 eV, and most of the remaining sulfur is addressed to sulfur ligands with a binding energy of 161.9 eV. Similar XPS results were obtained by Benck et al.[23] and Catalongue et al. [40] using in-line XPS.

From these results one explanation could be that the impression that the terminal $S_2^{2-}$ ligand is the most stable ligand in the amorphous material after two hours of measurement. However, the dramatic loss of exclusively bridging sulfur in our explanation should lead to a total disintegration of the $[Mo_3S_{12}]^{2-}$ clusters at the catalyst-electrolyte interface. Studying amorphous $MoS_3$, crystalline $MoS_2$ and $(NH_4)_2Mo_3S_{13}$ (ATM) by XPS, Weber et al.[38] found that the $S^{2-}$ atoms in hexagonal $MoS_2$ have the same binding energy as terminal $[S_2]^{2-}$ ligands in $[Mo_3S_{13}]^{2-}$ cluster. Thus, we interpret our XPS results as a transformation from an amorphous polymer chain structure consisting of $Mo_3S_{13}$ and $Mo_3S_{12}$ clusters to one that is composed of $MoS_2$ nano-islands.

In-situ / in-line Raman measurements

As proposed by Tran et al.[30], the $[S_2]^{2-}$ ligands of the $Mo_3S_{13}$ cluster are reduced and partly lost under potential bias in accordance with the $H_2S$ evolution observed in our DEMS experiment (see Fig. 7B). Loss of terminal $[S_2]^{2-}$ groups under $H_2S$ formation also agrees with our in-situ /in-line Raman measurements (see Fig. 9 and Fig. S12) and DFT calculations (see SI Supplementary Note 1), where a strong affinity of protons to react with terminal sulfur was found.

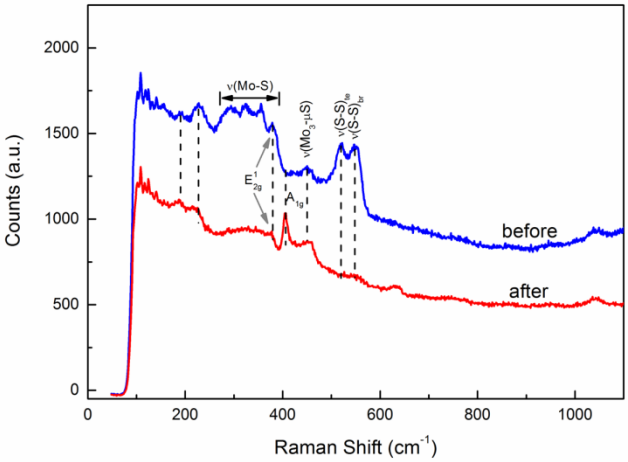


Figure 9. In-line Raman backscattering spectra of amorphous $MoS_x$ electrode before and after electrochemical cycling: as prepared $MoS_x$ electrode (blue curve) and $MoS_x$ after electrochemical cycling from -0.6 V to -2.1 V vs Pt (red curve).

The structural transformation of amorphous $MoS_x$ to a $MoS_2$ layer-type structure could be verified by Raman measurements in an *in-situ* cell. In this experiment, the spectrum of the sample was first measured through a quartz window without electrolyte (blue curve in Fig. 9). A different potential region (-0.6 V to -2.1V vs. Pt in a two-electrode system) was then chosen to accomplish a similar current density as obtained in CV results (see Fig. 3A). After filling the cell with electrolyte and electrochemical cycling, the *in-situ* chamber was flushed with deionized water and then dried by nitrogen gas to prevent oxidation. The Raman spectrum of the dried electrode after electrochemical treatment (red curve in Fig. 9) reveals that the vibrational modes of terminal and bridging $[S_2]^{2-}$ have almost completely disappeared. At the same time, a new vibrational mode emerges at 404 $cm^{-1}$ which can be assigned to the $A_{1g}$ mode of the layer structure of $MoS_2$. This result suggests a structural transformation of interlinked $Mo_3S_{12}$ - $Mo_3S_{13}$ moieties to $MoS_2$.

As shown above, the transformation leads to an improvement of the catalytic activity after 10 minutes cycling of the electrode (see the improvement of current density in Fig. 3A and the $H_2^+$ signal in Fig. 7). The Raman spectrum of the sample after being exposed to air is shown in Fig. S13. The broad feature with a peak position at ~955 $cm^{-1}$ can be interpreted as a hydrogenated $MoO_3$.[41] This interpretation is consistent with the occurrence of the $Mo^{6+}$ peak in Figs. 8C and E.

In literature, Li et al. [42] also studied the activation of $MoS_3$ HER catalyst after electrochemical cycling. The

authors came to the conclusion using high resolution transmission electron microscopy (HRTEM) and electron energy loss spectroscopy (EELS) that the material partially crystalized but their results suggest the amorphous $MoS_2$ is the catalytic active phase while the crystalline phase rather contributes to catalyst deactivation.

Electrochemical processes and layer transformation

It is assumed that under electrochemical conditions the $[S_2]^{2-}$ units present in polymerized $Mo_3S_{12}$ and $Mo_3S_{13}$ clusters are reduced to $S^{2-}$ when reacting with electrons under cathodic polarization. The reaction of electrons with protons and $[S_2]^{2-}$ entities will lead to the formation of $H_2S$ molecules. This transformation can be formulated by the equations:

$$Mo_3([S_2])_6 + 12H^+ + 12e^- \Rightarrow Mo_3(S)_6 + 6H_2 \quad \text{eq. (5)}$$

$$Mo_3(S)_6 + 4H^+ + 4e^- \Rightarrow (Mo_3([S]_4[\square]_2) + 2H_2S \quad \text{eq. (6)}$$

Symbol □ stands for an empty position where the original sulfur atom sited which has been released as $H_2S$. A possible mechanism to explain the reaction of protons at the edges of polymerized chains of $Mo_3S_{12}$ and $Mo_3S_{13}$ clusters under formation of $H_2S$ gas molecules is shown in Figure 10. The formation of $MoS_2$ islands after sulfur loss is illustrated in Figure 11. Here, the $MoS_2$ fragments that are formed likely include sulfur defects at the edges of nano-size S-Mo-S islands (see Fig. S15). The presence of these unsaturated Mo atoms leads to the formation of molybdenum hydride moieties under cathodic potential also proposed by Tran et al.[30]

In our model, the catalytic centers in nano-sized sulfur-defective $MoS_{2-x}$ islands are similar to those in larger $MoS_2$ particles where dangling bonds, i.e. coordinatively unsaturated bonds, are thought to be the catalytically active centers. *In-situ* Raman spectra show that the terminal sulfur species are the first ones to be removed under electrochemical cycling (SI Fig. S10). From this we conclude that $[S_2]^{2-}$ ligands are reduced to $S^{2-}$ and/or eliminated as $H_2S$ under turnover conditions.

The disappearance of terminal $[S_2]^{2-}$ and the reduction of bridging $[S_2]^{2-}$ to two $S^{2-}$ is leading to coordinatively unsaturated $Mo^{4+}$ atoms, i.e., dangling bonds at molybdenum atoms at the edges of S-Mo-S layers. The loss of sulfur at the edges under $H_2S$ release can be expressed by the eqs. (7) and (8):

$$MoS_2 + 2e^- + 2H^+ \rightarrow Mo[HS]_2 \quad \text{eq. (7)},$$

$$MoS_2 + 2e^- + 2H^+ \rightarrow Mo\text{-}(S\text{-}\square) + H_2S \quad \text{eq. (8)}.$$

In Fig. 10 these reactions are displayed in three steps: in the first step terminal [S2]2- units (see top of Fig. 10) are reduced to two $S^{2-}$ ligands (middle part of Fig. 10). One of these reduced terminal sulfur atoms then immediately reacts with two $H^+$ ions under formation of $H_2S$ (eq. (8)). It is also possible that a $[HS\text{-}HS]^{2-}$ unit is formed which reacts under reduced conditions to $H_2$ and $[S2]^{2-}$.

**Table 1. Peak positions of Mo 3d and S 2p XPS features and Mo - S as well as $Mo^{6+}$ – $Mo^{4+}$ ratios deviated from the measurements.**

| $MoS_x$ electrode | $Mo^1$ $3d_{5/2}$ (eV) | $Mo^2$ $3d_{5/2}$ (eV) | S 2s (eV) | $S_{terminal}$ $2p_{3/2}$ (eV) | $S_{bridging}$ $2p_{3/2}$ (eV) | $S_{other}$ $2p_{3/2}$ (eV) | Mo/S ratio | $Mo^{6+}/Mo^{4+}$ ratio |
|---|---|---|---|---|---|---|---|---|
| **As-prepared** | 229.1 | 232.3 | 227.2 | 161.9 | 163.0 | 163.5 | 1 : 3.97 | ---------- |
| **after CV for 10min** | 229.3 | 232.5 | 226.8 | 161.9 | 163.0 | 163.5 | 1 : 1.84 | 1 : 4.56 |
| **After CV for 2h** | 229.5 | 232.7 | 226.1 | 161.9 | 163.0 | 163.5 | 1 : 1.37 | 1 : 3.14 |

As $MoS_2$ fragments have been formed, the release of $H_2S$ stops. A possible mechanism is described in eqs. (9)-(11):

$$Mo\text{-}(S\text{-}\square) + e^- + H^+ \Leftrightarrow Mo\text{-}(S\text{-}H^*) \quad \text{eq. (9)},$$

$$Mo\text{-}(S\text{-}H^*) + e^- + H^+ \Leftrightarrow Mo\text{-}(S\text{-}\square) + H_2 \quad \text{eq.(10)}$$

$$2Mo\text{-}(S\text{-}H^*) \Leftrightarrow Mo\text{-}(S\text{-}\square) + H_2 \quad \text{eq.(11)}$$

An unsaturated molybdenum bond at the edge of a nano-island reacts with a proton from the electrolyte and an electron from the cathode at the electrode/electrolyte interface to a Mo-H* unit (eq. (9)). In a next step, Mo-H* reacts with a second proton and a second electron under formation of an $H_2$ gas molecule (see eq. (10)). Another possible path is assuming two Mo-H* units close to each other which can form one hydrogen molecule and leave two empty bonds on the surface (eq. (11)).

This reaction mechanism is illustrated in Fig. 11 in three steps (a): reaction of a negatively charged unsaturated bond of Mo, (b) reaction with a proton und formation of Mo-H* and (c) reaction of Mo-H* with a further proton and as second electron under $H_2$ formation or two Mo-H* units react together forming one $H_2$ molecule which is not shown in this figure. The transformation of amor-

phous $MoS_x$ to $MoS_2$ is supported by results described by Casalongue et al.[40] presenting DFT calculations which model the edge structure of $MoS_{2-x}$. They propose that the edges are terminated by S monomers, which are depicted in our model as $S^{2-}$ entities adjacent to a sulfur vacancy (see Fig. 11).

To summarize, during electrochemical cycling in the voltage range of 0.2 V to -0.3 V, the chain (Fig. 10) continuously transforms under release of $H_2S$ into a $MoS_2$ layer-type structure (see Fig. 11). Gray areas in Fig. 10 are representing polymerized chains of $Mo_3S_{12}$ and $Mo_3S_{13}$ units, yellow areas the acidic electrolyte in contact with $MoS_x$. At the interphase $[S_2]^{2-}$ units will be reduced and react under cathodic conditions with protons. Finally, $H_2S$ and $H_2$ gas molecules will be released from the $MoS_x$ chains as shown in the lower part.

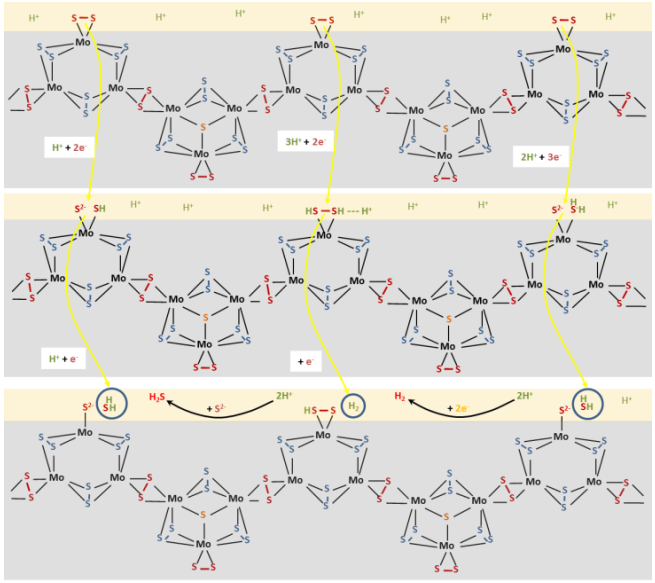

Figure 10. Structure of a chain consisting of polymerized $Mo_3S_{12}$ and $Mo_3S_{13}$ moieties that are present in $MoS_x$ films prepared by sputtering at RT.

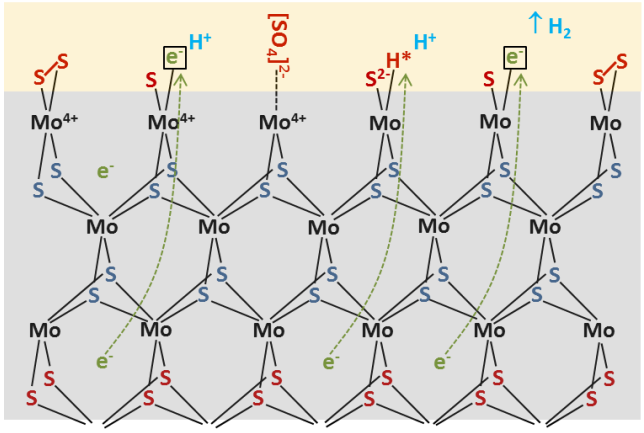


Figure 11. $MoS_2$ nano-island developed by reaction of polymer chains under release of $H_2S$. At the edges of the islands $H_2$ is formed in steps (see a), b) and c)) as expressed in eqs. (9) and (10). Also the reaction of $[SO_4]^{2-}$ ions with Mo is shown.

The presented model is supported by the fact that the cathode layer reacts with oxygen quickly under formation of $Mo^{6+}$ after exposure to an ambient atmosphere since the edge Mo atoms with dangling bonds would be easily oxidized in air rather than Mo atoms bonded to sulfur atoms. The $Mo^{4+}$: $Mo^{6+}$ ratio is given in Table 1. Assuming that all oxidized Mo atoms are located at the edges of S-Mo-S units, the size of the nano-islands can be approximately estimated from the ratio of $Mo^{6+}/Mo^{4+}$. After 10-20 minutes cycling, a cluster size of about 931 atoms (331 Mo atoms and 600 S atoms) can be assumed. After 2h exposure time, catalyst with cluster sizes of 363 atoms (169 Mo atoms and 294 S atoms) could be present. The details of the calculation are given in the Supporting Information, Supplementary Note 2. These considerations support the idea that the cluster size of the $MoS_{2-x}$ decreases during the electrochemical measurement. The size of the $MoS_2$ cluster after structural transformation can also explain the high ECSA and the low overpotential of the activated $MoS_x$.

## Conclusion

Molybdenum sulfide layers have been deposited on FTO substrates by reactive magnetron sputtering using an $Ar/H_2S$ gas atmosphere. The sputtered layers exhibit an increasing degree of crystallinity with increasing substrate temperature. Best performance is achieved by electrodes sputtered at room temperature which are originally amorphous. After electrochemical activation, they exhibit an overpotential of 180 mV at a current density of $-10\ mAcm^{-2}$, which is amongst the highest hydrogen evolution activities ever reported for $MoS_x$. The stability of the electrodes was tested for 10 h and showed an increase in overpotential of 4.6 mV/h.

The structure of amorphous $MoS_x$ contains in the beginning of polymerized $[Mo_3S_{12}]^{2-}$ and $[Mo_3S_{13}]^{2-}$ entities as known from crystalline $(NH_4)_2Mo_3S_{13}$. DEMS result reveals that the activation is accompanied by the evolution of $H_2S$. Combining results from Raman and X-ray photoelectron spectroscopy show that the loss of sulfur is accompanied by a structural transformation from the amorphous material to a layer-type $MoS_{2-x}$ structure. Thus, the catalytic activity is no longer exclusively determined by the presence of $[Mo_3S_{13}]^{2-}$ clusters, but is due to the formation of $MoS_2$ nano-island exhibiting a high number of sulfur defects leading to coordinatively unsaturated Mo atoms found at the edges of S-Mo-S layers. A reaction mechanism is proposed in which Mo atoms with dangling bonds located at the edges act as the catalytically active sites. The proposed mechanism offers new insights that may help to further improve the activity and stability of this promising earth-abundant hydrogen evolution catalyst.

## ASSOCIATED CONTENT

## SUPPORTING INFORMATION

Scheme of sputtering chamber, scheme of *in-situ* Raman cell, DEMS cell, photos of samples, XRD patterns, CV scans, Raman spectra, SEM images, DFT calculations, Particle size calculations and determinations.

## Author Information

### Corresponding Author

*fanxing.xi@helmholtz-berlin.de and *fiechter@helmholtz-berlin.de

## Acknowledgments

F.X. and S.F. acknowledges the financial support by the German Research Association (DFG) in the Priority Program SPP1613 under contract # FI 1524/4-2, entitled "Development of catalysts, namely manganese oxides and molybdenum sulfides, for an implementation in a light-driven water splitting device using a multi-junction solar cell". X.H. acknowledges the use of the UCL Grace High Performance Computing Facility (Grace@UCL), and associated support services and financial support by EPSRC (EP/No32888/1).

## References

1. Tran, P. D.; Wong, L. H.; Barber, J.; Loo, J. S. C., Recent advances in hybrid photocatalysts for solar fuel production. *Energy & Environmental Science* **2012,** 5 (3), 5902.
2. P.J.Boddy, Oxygen evolution on semiconducting TiO2. *Journal of The Electrochemical Society* **1968,** *115* (2), 199-203.
3. Fujishima Akira, H. K., Electrochemical Photolysis of Water at a Semiconductor Electrode. *Nature* **1972,** *238* (5358), 37-38.
4. Gary, H. B., Powering the planet with solar fuel. *Nature Chemistry* **2009,** *1* (1), 7-7.
5. McCrory, C. C.; Jung, S.; Ferrer, I. M.; Chatman, S. M.; Peters, J. C.; Jaramillo, T. F., Benchmarking hydrogen evolving reaction and oxygen evolving reaction electrocatalysts for solar water splitting devices. *J Am Chem Soc* **2015,** *137* (13), 4347-57.
6. Merki, D.; Hu, X., Recent developments of molybdenum and tungsten sulfides as hydrogen evolution catalysts. *Energy & Environmental Science* **2011,** *4* (10), 3878.
7. Yang, S.; Gong, Y.; Zhang, J.; Zhan, L.; Ma, L.; Fang, Z.; Vajtai, R.; Wang, X.; Ajayan, P. M., Exfoliated graphitic carbon nitride nanosheets as efficient catalysts for hydrogen evolution under visible light. *Adv Mater* **2013,** *25* (17), 2452-6.
8. (a) Kibsgaard, J.; Tsai, C.; Chan, K.; Benck, J. D.; Nørskov, J. K.; Abild-Pedersen, F.; Jaramillo, T. F., Designing an improved transition metal phosphide catalyst for hydrogen evolution using experimental and theoretical trends. *Energy & Environmental Science* **2015,** *8* (10), 3022-3029; (b) Popczun, E. J.; McKone, J. R.; Read, C. G.; Biacchi, A. J.; Wiltrout, A. M.; Lewis, N. S.; Schaak, R. E., Nanostructured nickel phosphide as an electrocatalyst for the hydrogen evolution reaction. *J Am Chem Soc* **2013,** *135* (25), 9267-70; (c) Xiao, P.; Sk, M. A.; Thia, L.; Ge, X.; Lim, R. J.; Wang, J.-Y.; Lim, K. H.; Wang, X., Molybdenum phosphide as an efficient electrocatalyst for the hydrogen evolution reaction. *Energy Environ. Sci.* **2014,** *7* (8), 2624-2629.
9. (a) Voiry, D.; Yamaguchi, H.; Li, J.; Silva, R.; Alves, D. C.; Fujita, T.; Chen, M.; Asefa, T.; Shenoy, V. B.; Eda, G.; Chhowalla, M., Enhanced catalytic activity in strained chemically exfoliated WS(2) nanosheets for hydrogen evolution. *Nat Mater* **2013,** *12* (9), 850-5; (b) Bonde, J.; Moses, P. G.; Jaramillo, T. F.; Norskov, J. K.; Chorkendorff, I., Hydrogen evolution on nano-particulate transition metal sulfides. *Faraday Discussions* **2008,** *140*, 219-231; (c) Kornienko, N.; Resasco, J.; Becknell, N.; Jiang, C. M.; Liu, Y. S.; Nie, K.; Sun, X.; Guo, J.; Leone, S. R.; Yang, P., Operando spectroscopic analysis of an amorphous cobalt sulfide hydrogen evolution electrocatalyst. *J Am Chem Soc* **2015,** *137* (23), 7448-55.
10. (a) Liao, L.; Wang, S.; Xiao, J.; Bian, X.; Zhang, Y.; Scanlon, M. D.; Hu, X.; Tang, Y.; Liu, B.; Girault, H. H., A nanoporous molybdenum carbide nanowire as an electrocatalyst for hydrogen evolution reaction. *Energy Environ. Sci.* **2014,** *7* (1), 387-392; (b) Chen, W. F.; Muckerman, J. T.; Fujita, E., Recent developments in transition metal carbides and nitrides as hydrogen evolution electrocatalysts. *Chem Commun (Camb)* **2013,** *49* (79), 8896-909; (c) Wan, C.; Regmi, Y. N.; Leonard, B. M., Multiple phases of molybdenum carbide as electrocatalysts for the hydrogen evolution reaction. *Angew Chem Int Ed Engl* **2014,** *53* (25), 6407-10.
11. Lee, Y. H.; Zhang, X. Q.; Zhang, W.; Chang, M. T.; Lin, C. T.; Chang, K. D.; Yu, Y. C.; Wang, J. T.; Chang, C. S.; Li, L. J.; Lin, T. W., Synthesis of large-area MoS2 atomic layers with chemical vapor deposition. *Adv Mater* **2012,** *24* (17), 2320-5.
12. S. Helveg, J. V. L., E. Lægsgaard, I. Stensgaard, J. K. Nørskov, B. S. Clausen, H. Topsøe, and F. Besenbacher, Atomic Scale Structure of Single-Layer MoS2 Nanoclusters. *Physical Review Letters* **2000,** *84* (5), 951.
13. H.Tributsch, J. C. B., Electrochemistry and photochemistry of MoS2 layer crystals. I. *Journal of Electroanalytical Chemistry and Interfacial Electrochemistry* **1977,** *81* (1), 97-111.
14. H.Tributsch, Solar Energy-Assisted Electrochemical Splitting of Water. Some Energetical Kinetical and Catalytical Considerations Verified on MoS2 Layer Crystal Surfaces. *Zeitschrift für Naturforschung A* **1977,** *81* (1), 97-111.
15. (a) Benck, J. D.; Hellstern, T. R.; Kibsgaard, J.; Chakthranont, P.; Jaramillo, T. F., Catalyzing the Hydrogen Evolution Reaction (HER) with Molybdenum Sulfide Nanomaterials. *Acs Catalysis* **2014,** *4* (11), 3957-3971; (b) Jakob Kibsgaard; Jaram, T. F., Molybdenum Phosphosulfide An Active, Acid-Stable, Earth-Abundant Catalyst for the Hydrogen Evolution Reaction. *Angewandte Chemie International Edition* **2014,** 53 (52), 14433-14437.
16. Berit Hinnemann, P. G. M., Jacob Bonde,Kristina P. Jørgensen,Jane H. Nielsen,Sebastian Horch,Ib Chorkendorff, andJens K. Nørskov, Biomimetic Hydrogen Evolution MoS2 Nanoparticles as Catalyst for Hydrogen Evolution. *JOURNAL OF THE AMERICAN CHEMICAL SOCIETY* **2005,** *127* (15), 5308-5309.
17. Kiriya, D.; Lobaccaro, P.; Nyein, H. Y.; Taheri, P.; Hettick, M.; Shiraki, H.; Sutter-Fella, C. M.; Zhao, P.; Gao, W.; Maboudian, R.; Ager, J. W.; Javey, A., General Thermal Texturization Process of MoS2 for Efficient Electrocatalytic Hydrogen Evolution Reaction. *Nano Lett* **2016,** *16* (7), 4047-53.
18. Choi, Y.-H.; Cho, J.; Lunsford, A. M.; Al-Hashimi, M.; Fang, L.; Banerjee, S., Mapping the electrocatalytic activity of MoS2 across its amorphous to crystalline transition. *J. Mater. Chem. A* **2017,** 5 (10), 5129-5141.
19. Jaramillo, T. F.; Jorgensen, K. P.; Bonde, J.; Nielsen, J. H.; Horch, S.; Chorkendorff, I., Identification of active edge sites for electrochemical H-2 evolution from MoS2 nanocatalysts. *Science* **2007,** *317* (5834), 100-102.
20. Kibsgaard, J.; Chen, Z.; Reinecke, B. N.; Jaramillo, T. F., Engineering the surface structure of MoS2 to preferentially expose active edge sites for electrocatalysis. *Nat Mater* **2012,** *11* (11), 963-9.
21. Li, H.; Tsai, C.; Koh, A. L.; Cai, L.; Contryman, A. W.; Fragapane, A. H.; Zhao, J.; Han, H. S.; Manoharan, H. C.; Abild-Pedersen, F.; Norskov, J. K.; Zheng, X., Activating and optimizing MoS2 basal planes for hydrogen evolution through the formation of strained sulphur vacancies. *Nat Mater* **2016,** *15* (1), 48-53.
22. Morales-Guio, C. G.; Hu, X., Amorphous molybdenum sulfides as hydrogen evolution catalysts. *Acc Chem Res* **2014,** *47* (8), 2671-81.
23. Benck, J. D.; Chen, Z.; Kuritzky, L. Y.; Forman, A. J.; Jaramillo, T. F., Amorphous Molybdenum Sulfide Catalysts for Electrochemical Hydrogen Production: Insights into the Origin of their Catalytic Activity. *ACS Catalysis* **2012,** *2* (9), 1916-1923.
24. Merki, D.; Fierro, S.; Vrubel, H.; Hu, X., Amorphous molybdenum sulfide films as catalysts for electrochemical hydrogen production in water. *Chem. Sci.* **2011,** *2* (7), 1262-1267.
25. Shin, S.; Jin, Z.; Kwon, D. H.; Bose, R.; Min, Y. S., High turnover frequency of hydrogen evolution reaction on amorphous MoS2 thin film directly grown by atomic layer deposition. *Langmuir* **2015,** *31* (3), 1196-202.
26. Kibsgaard, J.; Jaramillo, T. F.; Besenbacher, F., Building an appropriate active-site motif into a hydrogen-evolution catalyst with thiomolybdate Mo3S13 (2-) clusters. *Nature Chemistry* **2014,** *6* (3), 248-253.
27. Prof. Dr. Achim Müller; Dr. Sabyasachi Sarkar; Dr. Ram Gopal Bhattacharyya; Dr. Siegfried Pohl; Dartmann, M., Directed

Synthesis of [Mo3S13] 2–, an Isolated Cluster Containing Sulfur Atoms in Three Different States of Bonding. *Angewandte Chemie* **1978,** *17* (7), 535.
28. P.Bogdanoff, N. A.-V., A kinetic approach of competitive photoelectrooxidation of HCOOH and H2O on TiO2 anatase thin layers via on-line mass detection. *Journal of Electroanalytical Chemistry* **1994,** *379* (1-2), 415-421.
29. Shu Min Tan; Dr. Adriano Ambrosi; Prof. Zdeněk Sofer; Štěpán Huber; Prof. David Sedmidubský; Pumera, P. M., Pristine Basal- and Edge-Plane-Oriented Molybdenite MoS2 Exhibiting Highly Anisotropic Properties. *Chemistry-A European Journal* **2015,** *21* (19), 7170-7180.
30. Tran, P. D.; Tran, T. V.; Orio, M.; Torelli, S.; Truong, Q. D.; Nayuki, K.; Sasaki, Y.; Chiam, S. Y.; Yi, R.; Honma, I.; Barber, J.; Artero, V., Coordination polymer structure and revisited hydrogen evolution catalytic mechanism for amorphous molybdenum sulfide. *Nat Mater* **2016,** *15* (6), 640-6.
31. Ambrosi, A.; Pumera, M., Templated Electrochemical Fabrication of Hollow Molybdenum Sulfide Microstructures and Nanostructures with Catalytic Properties for Hydrogen Production. *ACS Catalysis* **2016,** *6* (6), 3985-3993.
32. Bockris, J. M., Potter, E. C., The mechanism of the cathodic hydrogen evolution reaction. *Journal of The Electrochemical Society* **1952,** *99* (4), 169-186.
33. Fletcher, S., Tafel slopes from first principles. *Journal of Solid State Electrochemistry* **2008,** *13* (4), 537-549.
34. Merki, D.; Vrubel, H.; Rovelli, L.; Fierro, S.; Hu, X., Fe, Co, and Ni ions promote the catalytic activity of amorphous molybdenum sulfide films for hydrogen evolution. *Chemical Science* **2012,** *3* (8), 2515.
35. B.E. Conway, B. V. T., Interfacial processes involving electrocatalytic evolution and oxidation of H 2, and the role of chemisorbed H. *Electrochimica Acta* **2002,** *47* (22), 3571-3594.
36. Allen J. Bard, L. R. F., Electrochemical Methods: Fundamentals and Applications. *Wiley: New York* **2001**.
37. Benson, J.; Li, M.; Wang, S.; Wang, P.; Papakonstantinou, P., Electrocatalytic Hydrogen Evolution Reaction on Edges of a Few Layer Molybdenum Disulfide Nanodots. *ACS Appl Mater Interfaces* **2015,** *7* (25), 14113-22.
38. Weber T, M. J. C., Niemantsverdriet J W, Structure of amorphous MoS3. *The journal of Physical Chemistry* **1995,** *99* (22), 9194-9200.
39. Muijsers J.C., W. T., van Hardeveld R.M., Zandbergen H. W., Niemantsverdriet J. W., XPS Sulfidation Study of Molybdenum Oxide Using MoO3SiO2Si(100) Model Catalysts and Mo-IV3-Sulfur Cluster *Journal of Catalysis* **1995,** *157* (2), 698-705.
40. Casalongue, H. G. S.; Benck, J. D.; Tsai, C.; Karlsson, R. K. B.; Kaya, S.; Ng, M. L.; Pettersson, L. G. M.; Abild-Pedersen, F.; Nørskov, J. K.; Ogasawara, H.; Jaramillo, T. F.; Nilsson, A., Operando Characterization of an Amorphous Molybdenum Sulfide Nanoparticle Catalyst during the Hydrogen Evolution Reaction. *The Journal of Physical Chemistry C* **2014,** *118* (50), 29252-29259.
41. L Seguin, M. F., R Cavagnat, J.-CLassègues, Infrared and Raman spectra of MoO3 molybdenum trioxides and MoO3· xH2O molybdenum trioxide hydrates. *Spectrochimica Acta Part A: Molecular and Biomolecular Spectroscopy* **1995,** *51* (8), 1323-1344.
42. Lee, S. C.; Benck, J. D.; Tsai, C.; Park, J.; Koh, A. L.; Abild-Pedersen, F.; Jaramillo, T. F.; Sinclair, R., Chemical and Phase Evolution of Amorphous Molybdenum Sulfide Catalysts for Electrochemical Hydrogen Production. *ACS Nano* **2016,** *10* (1), 624-32.